Robust, Transparent Hybrid Thin Films of Phase-Change Material Sb 2 S 3 Prepared by Electrophoretic Deposition

Christopher L Hassam, Flavien Sciortino, Ngan T.K. Nguyen, Bhuvanesh Srinivasan, Katsuhiko Ariga, Franck Gascoin, Fabien Grasset, Takao Mori, Tetsuo Uchikoshi, Yohann Thimont, et al.

Robust, transparent hybrid thin films of phase-change material Sb_2S_3 prepared by electrophoretic deposition

*Christopher L. Hassam[1,2,3,4], Flavien Sciortino[3], Ngan T.K. Nguyen[1,4], Bhuvanesh Srinivasan[1,3], Katsuhiko Ariga[3,5], Franck Gascoin[2], Fabien Grasset[1,6], Takao Mori [1,3,7], Tetsuo Uchikoshi[1,4], Yohann Thimont[8], David Berthebaud[1]**

[1] CNRS-Saint Gobain-NIMS, IRL 3629, Laboratory for Innovative Key Materials and Structures (LINK), National Institute for Materials Science (NIMS), Tsukuba, 305-0044, Japan

[2] Laboratoire CRISMAT UMR 6508 CNRS ENSICAEN UCBN, 6 Boulevard du Maréchal Juin, 14050, Caen Cedex 04, France

[3] WPI International Center for Materials Nanoarchitechtonics (WPI-MANA), National Institute for Materials Science (NIMS), Namiki 1-1, Tsukuba, 305-0044, Japan

[4] National Institute for Materials Science, 1-2-1 Sengen, Tsukuba, Ibaraki 305-0047, Japan

[5] Department of Advanced Materials Science, Graduate School of Frontier Sciences, The University of Tokyo, 5-1-5 Kashiwanoha, Kashiwa, Chiba 277-8561, Japan

[6] Univ. Rennes – CNRS – Institut des Sciences Chimiques de Rennes, UMR 6226, 35000 Rennes, France

[7] Graduate School of Pure and Applied Sciences, University of Tsukuba, Tennodai 1-1-1, Tsukuba 305-8671, Japan

[8] CIRIMAT, Université de Toulouse, CNRS, Université Toulouse 3 - Paul Sabatier, 118 Route de Narbonne, 31062 Toulouse cedex 9, France

*Corresponding author: David.BERTHEBAUD@cnrs.fr

Keywords

Coating materials, Thin films, Chalcogenides, Electrophoretic deposition, Phase change materials

Abstract

Thin films of polyethyleneimine-stabilized Sb_2S_3 are prepared via electrophoretic deposition (EPD), showing strong adhesion between deposited layers and underlying substrate, with the films being crystallized via annealing. For amorphous films, thicknesses can be freely tuned from 0.2-1 μm, shrinking to 0.1-0.5 μm when crystallized, whilst retaining a crack- and defect-free surface, thus not impacting on their good stability, and maintaining their optical properties. Through UV-Vis spectroscopy and subsequent modelling of the obtained spectra, it was concluded that the materials after annealing showed a reduced band gap and a demonstrably increased refractive index (n) and carrier concentration. The use of EPD for this material shows the viability of rapidly creating stable thin films of phase-change materials.

Introduction

Phase change materials (PCMs) have the capacity to undergo rapid, reversible changes between two or more stable phases with distinct optoelectronic properties.[1,2] The contrast between the

individual phase properties, the capacity to rapidly cycle between phases, and the stability of each individual phase are all key features required for the successful development and application of PCMs. Developing and optimizing new and existing PCMs, and improving processing techniques are active and important areas of research.[3–6]

Chalcogenide materials, those containing S, Se, or Te, are often PCMs.[2] Early use of their phase change properties led to the proliferation of optical storage media in the forms of three successive generations of rewriteable optical discs.[7] While the rapid advancement of electronic memory storage has reduced the viability of optical storage methods, there is a great deal of research interest in PCMs directed towards their use as non-volatile memory storage.[8,9]

The $(GeTe)_x(Sb_2Te_3)_{1-x}$ (GST) family of chalcogenides in particular are an example of the breadth of research undertaken on PCMs.[10–14] The material $Ge_2Sb_2Te_5$ is widely available and combines large optical and electronic property differences ($\Delta n>2$, $\Delta k>1$, $\Delta\rho>10^3\ \Omega\cdot m$) with a sub-nanosecond phase transition time, and relatively low transition temperature (~173 °C).[2,6] For non-volatile memory applications, the sharp decrease in resistivity upon crystallization is exploitable as logical states in non-volatile memory applications, whilst the optical property differences are being explored for their applications in integrated photonic devices, and for use as nanoscale displays.[10]

Whilst many successful applications of $Ge_2Sb_2Te_5$ have been explored and continue to be developed, significant challenges remain with the material owing to its absorbance in much of the visible and near-IR spectrum, with amorphous and crystalline band gaps of 0.5 and 0.7 eV respectively.[15] It is desirable that for a given wavelength region that whilst the change in refractive index is large, that both the extinction coefficient and the change in extinction coefficient is small, preventing energy loss to absorption as much as possible.[11,16] As these values cannot be altered

independently, and are particular to a given material, it follows that for each wavelength region there is a material which provides the optimal optical properties, defined by a figure-of-merit, conventionally calculated as $\Delta n/\Delta k$,[16] however, other figures of merit have been proposed depending on the criteria to be evaluated[3,17] material must be further judged for its other properties, such as phase stability and switching speed, and a judgement made on which material provides the best compromise of properties for the desired application. It is with this aim that an increasing section of research involves investigating alternative chalcogenides specialized for use in different wavelength regions. This exploration is considering materials both along the GeTe-Sb_2Te_3 semi-boundary line, as well as with the substitution of alternative elements. Germanium telluride is another example of a chalcogenide material experiencing significant interest,[5,18] with research driven not just by the large shift in its optical properties, but also by its additional potential use as a thermoelectric material.[19,20] A recently developed alternative chalcogenide for the telecommunications wavelength region (at around 1550 nm) is $Ge_2Sb_2Se_4Te_1$ (GSST) which improves upon the properties of GST through the substitution of Te with Se, and more generally, the potential improvements that could be found through the substitution of lighter elements, such as Se or S for Te.[11]

Exploiting the potential of the lighter chalcogenides, recently attention has been paid to antimony trisulfide, an optical PCM with band gaps variously reported in literature as between 1.7-2.7 eV (amorphous),[21,22] and 1.2-2.2 eV,[23–27]showing promise for applications in the visible region of the spectrum. Early research conducted on Sb_2S_3 in the 1990s concluded the material was unsuited for optical data storage.[28] However, current studies have revealed the potential it has for nanophotonic devices and in integrated photonic circuits.[3,29] Onset of crystallization occurs at a relatively low temperature ~250 °C,[11] leading to low processing temperatures, commonly between 250-300

°C,[30,31] and a low melting point of 550 °C,[32] allowing for stability in both phases, important for data retention,[33] whilst also being accessible by applicable heating methods, such as laser diode heating. It shows lower toxicity compared to its Se and Te equivalents, is composed of inexpensive, non-rare elements, and is rapidly synthesizable as nanoparticles via a number of different methods, including solid-state methods such as mechanical ball-milling, and wet-chemical methods such as hot injection.[34–36]

It is also worth noting, that ongoing research exists on non-chalcogenide families showing similar phase transitions with significant optical and resistive contrast. Vanadium dioxide is an example of a material which shows a low transition temperature (68 °C) and sub-nanosecond switching speeds.[37] However, compared to the heretofore defined PCMs, the heating-induced phase transition of VO_2 is reversible, rendering it unsuited for non-volatile applications.[8]

Thin film PCMs are an interesting target geometry with applications for non-volatile memory storage,[38] photovoltaics,[35] as well as nanoscale displays.[39] Intuitively, the most interesting feature of PCMs is their capacity to switch between phases rapidly and permanently (until switched back). Nanoparticulate PCMs, including thin films, show a number of scale-related effects beneficial to their application. These include an elevation of crystallization temperature (useful for increasing operating temperature without inducing undesired amorphous-crystalline transitions),[40] the reduction in the melting point (thus requiring lower energy for reset operations), and an increase in the surface-to-volume ratio (which, for the poorly thermally conductive materials, reduces the level of active cooling required during a reset operation).[39] It has been observed for PCMs that crystallization can occur either homogeneously or heterogeneously, with heterogeneous crystallization showing greater speed.[41] The reduction in particle size serves to increase the interface available, promoting heterogeneous crystallization, and enabling rapid switching speeds.[1]

Vacuum techniques such as radio frequency and magnetron sputtering are commonly used to prepare thin films of PCMs.[3,29,42] Other methods, including (metal-organic) chemical vapor deposition,[43] and electrochemical deposition,[44] have also been used to synthesize thin films of optical PCMs for various applications. Thin films based on pre-synthesized GeTe nanoparticles, spin-coated onto a surface have recently been reported, showing the capacity for size-tuning of the optical properties of the surface.[5] Spin coating enables rapid sample preparation, however, has limitations of scalability and geometry.

In comparison, electrophoretic deposition (EPD) is a method of depositing material onto a conductive surface with controllable thicknesses, ranging across orders of magnitude in size from nm – μm scale.[45] As a process it is simple, fast and able to be applied to a variety of conductive materials, surfaces and geometries. It has been successfully applied for developing anti-fog coatings,[46] photoelectrodes,[47] UV-blocking coatings for windows,[48] and anti-corrosive protective coatings.[49] In EPD the choice of solvent, the distance between the electrodes, the deposition time and applied voltage will affect the homogeneity of the deposited film.[45]

For successful deposition, the dispersed material must be charged, either intrinsically, or through the use of additives or dispersants. Adhesion between the deposited material and the substrate to which it is deposited is one of the keys in forming a film by EPD, often necessitating the use of binders to improve the film stability.[50] Use of such dispersion additives and binders, however, must be balanced against the application desired for the material, as their presence in the final product can affect the properties of the material formed.[45]

In this work, the wet chemical synthesis of Sb_2S_3, as reported by Yang *et al*.,[34] is adapted to produce nanoparticles of Sb_2S_3 capped by a polymeric agent, polyethyleneimine (PEI). For this application PEI was selected as it has no absorbance in the region of interest in the UV-visible

spectrum.[51] The subsequent use of these particles in producing particle-polymer hybrid thin films is described. Scheme 1 displays a schematic of the synthesis and film production. The thicknesses of these films are confirmed using a profilometer, and the UV-Vis-NIR spectra of the samples measured. Modelling of the spectra is conducted to extract values for the samples for the thicknesses, gap energies, optical index, plasma frequencies, carrier damping, and subsequently to determine the concentration and intrinsic mobility of the carriers in the Sb_2S_3 material for each thin film. These values were used to probe the effect of the EPD technique on the properties of thin films. Whilst thin films of antimony trisulfide have been presented before,[29,30] no work previously has shown the viability of using EPD as a method for developing these materials. This shows the potential of this technique for the future development of geometrically unique and conforming films of phase change material on surfaces of interest

.

Scheme 1. Above: cartoon representation, below: photographic representation, of experimental process, left to right: chemical synthesis, electrophoretic deposition, as-deposited film (SEM insert), annealed film (SEM insert).

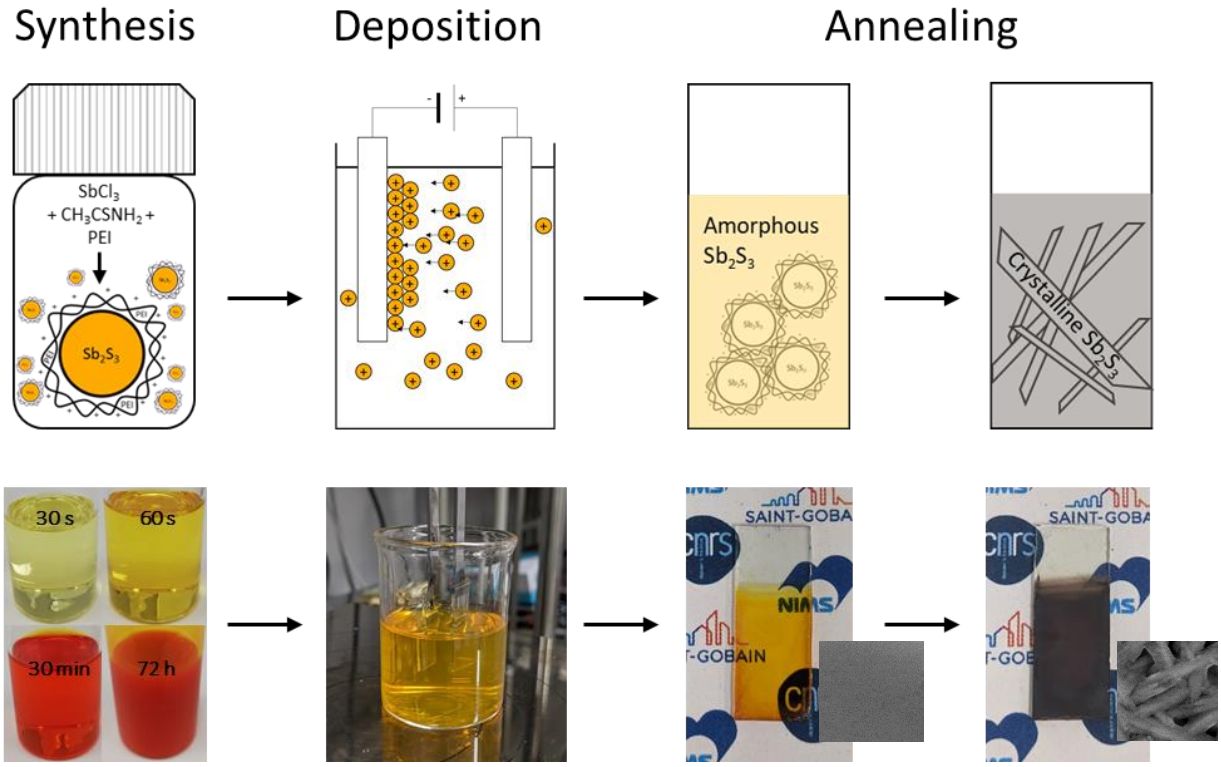

Methods

Reagents

Poly(ethyleneimine) (10000 MW), acetone (99.5 %), and methanol (99.8 %) were obtained from Wako. Ethylene glycol (99.8 %), antimony trichloride (>98 %) and thioacetamide (98 %) were obtained from Merck (Sigma-Aldrich). Reagents and solvents were used as received. Indium doped tin oxide (ITO) glass (10 Ω/sq) (Geomatec Co., Ltd., Japan) were used as substrates.

Synthesis

Polyethyleneimine (1.5 g) was dissolved in ethylene glycol (22.5 mL) by stirring for a minimum of 24 hours to form a stock solution. Antimony trichloride (0.235 g) and thioacetamide (0.160 g)

were separately dissolved in aliquots of the PEI stock solution (1 mL) and ethylene glycol (9 mL). After complete dissolution of both precursors, they were combined, shaken vigorously and allowed to sit for 24 hours.

To clean the particles, the reaction mixture was diluted with methanol (10 mL) and centrifuged (30 min, 11000 rpm) with an AS ONE centrifuge (AS185) equipped with a No. 4 6 x 50 mL rotor (radius 9.5 cm). The precipitate was collected and redispersed in methanol (15 mL), before centrifugation under the same conditions. This was repeated once more. The final precipitate was collected and redispersed in methanol (20 mL), and taken as a stock solution. Gravimetric determination of the concentration was undertaken by separating three 0.5 mL aliquots of stock solution into pre-weighed weighing vessels. The aliquots were dried at 80 degrees under vacuum overnight to remove solvent, with a final concentration determined of 4.3 $mg \cdot ml^{-1}$.

For preparing dispersions for EPD, a 4 mL aliquot of this dispersion was diluted with methanol (6 mL), and sonicated and stirred for 1 hour. After this, acetone (10 mL) was added to the dispersion, and stirred for a further 15 minutes. The acetone:methanol dispersion was then used for EPD.

The ITO glass was cut into (2 x 1) cm rectangles. To clean, the substrates were immersed in deionized water with non-ionic detergent and sonicated for 15 minutes, before rinsing with water and sonication for an additional 15 minutes. Then, the substrates were sonicated in ethanol for two 15-minute periods, and then acetone for two 15-minute periods.

For deposition, 10 V is applied between electrodes separated by 5 mm, for periods ranging between 10 seconds to 10 minutes. A Keithley Model 2400 (Keithley, USA) was used as the electric field generator. Significant optimization is required to achieve appropriate films via EPD, with higher voltages tried resulting in significantly more cracking in the films, while lower

voltages resulted in little-to-no film formation during the deposition, even with extended deposition times. Once deposited, films were annealed under vacuum at 300 °C for between 30 min to 2 hours.

Characterization

Zeta potential measurements of the sample in methanol were taken using a Malvern Zetasizer Nano Z (Malvern Instruments Ltd., UK). Dynamic light scattering (DLS) measurements of the sample in methanol were taken with an ELSZ-2000ZS (Otsuka Electronics Co. ltd., Japan), using a cumulant method. Concentrations of the samples were 0.9 $mg \cdot mL^{-1}$ and the effective pH in methanol was 7.80. Film thicknesses were measured using a DektakXT stylus profiler (Bruker Co., USA). Raman scattering spectra were recorded using a T64000 Raman spectrometer (HORIBA Jobin Yvon SAS, France) with a laser wavelength of 514.5 nm.

Powder XRD measurements were taken using a θ-θ Rigaku SmartLab 3 diffractometer (Rigaku, Japan) with Cu-Kα radiation from 10 to 90°, with a 0.02° step width, and scan speed of $2° \cdot min^{-1}$. Film XRD measurements were taken using a Rigaku SmartLab (Rigaku, Japan) (from 10 to 70°, with a 0.04° step width, and a scan speed of $2° \cdot min^{-1}$). The Rietveld method was used for the full-profile fitting of XRD patterns obtained, performed using WinPlotr, within the FullProf software suite.[52–54] The peak shapes were modelled using a Thomson-Cox-Hastings pseudo-Voigt function, the background was estimated manually and the zero-point shift and asymmetry parameters were refined. The lattice parameters, fractional atomic coordinates and the overall displacement parameter (B_{ov}) were sequentially refined to obtain the final profile.

UV-Vis transmittance measurements were taken using a V-770 UV-Vis-NIR spectrophotometer (JASCO Co., Japan). Modelling of the transmittance spectra of the films was undertaken using the SCOUT software.[55] Firstly, the uncoated ITO glass was implemented using

a glass substrate dielectric model and a conventional ITO dielectric model (with a refinement of the plasma frequency and damping of the Drude model for the ITO layer). A dielectric function of the Sb_2S_3 material was made using three contributions: a dielectric background, an interband Kramer-Kronig Relation susceptibility (to integrate the gap energy),[56] and a Drude model (to include plasma frequency and damping) used for the free carrier contribution.

For SEM and EDX measurements of free powder, a tabletop TM-3000 SEM (Hitachi High-Tech Co., Japan) was used with an accelerating voltage of 15 kV. Morphology of films was investigated using a S-4800 FE-SEM apparatus (Hitachi, Japan) at an accelerating voltage of 10 kV. Chemical mapping of films was performed at an accelerating voltage of 10 kV using a SU-8000 FE-SEM (Hitachi High-Tech Co., Japan) equipped with a Bruker EDX detector (Bruker Nano GmbH, Germany).

A schematic diagram of the impedance measurement setup is presented in Figure S-1. For photoelectric measurements, two films deposited on ITO-coated glass (total deposition time, 5 minutes). These films were placed into contact with each other, with a total measurement area of 1 cm^2. Illumination was generated by a MAX-303, 300 W compact Xenon light source (Asahi Spectra Co., Ltd.). A monochromator combined with an optical filter (Transmittance ~ 80 %) was used to generate monochromatic light with peaks centered at 370, 440, 540, and 580 nm with bandwidths of approximately 10 nm. A Keithley Model 2400 source meter (Keithley, USA) was used to measure the photocurrent response of the films at biases of 0.5 and 1 V under ambient condition.

Results and Discussion

Upon combination of the $SbCl_3$ and thioacetamide solutions, the reaction mixture rapidly turned yellow due to the formation of HS^- in solution and then orange from the formation of Sb_2S_3,

remaining transparent for a period of hours. After 24 hours the sample was opaque, orange, and free flowing. No change in the sample was noted after 24 hours, with the lack of precipitation suggesting the stability of the suspension.

Different conditions and capping agents (including PEI, polystyrenesulfonate, polyethyleneglycol, citric acid, oleylamine, dodecyltrimethylammonium bromide, and thioglycolic acid) were tested to optimize the particle synthesis, however adding PEI into the initial reaction was found to be the only condition that resulted in a stable dispersion. When other capping agents or no capping agents, or stabilization by pH adjustments were used, it resulted in an unstable dispersion, with either oxidation or precipitation occurring during the reaction (supplementary information, Figure S-2). If no capping agent was introduced in the synthesis, a red precipitate was generated, agreeing with the syntheses undertaken by Yang *et al*.,[34] While the dispersion was stable in ethylene glycol, a successful film could not be produced via EPD, as the films could not be dried quickly at room temperature. Cleaning of the reaction was undertaken using methanol in order to transfer the dispersion into a lower-boiling point solvent compatible with EPD. Water, ethanol and isopropanol were found to be unsuitable solvents, resulting in precipitation of the material. The precipitate in isopropanol exhibited a colour change from orange to white, indicating the formation of antimony oxide.

Samples were dried in order to assess the success of the synthesis. When dried under atmosphere on a poorly-wetting surface, the PEI-capped Sb_2S_3 appeared as dark red needles, turning dark grey upon annealing (supplementary information, Figure S-3). The diffractogram obtained for the non-annealed sample (Figure 1a) showed broad features characteristic of scattering from an amorphous sample, as expected. Comparatively, the diffractogram of the annealed samples (Figure 1b)

showed sharp peaks, all of which were attributed to Sb_2S_3. No peaks were observed that could indicate the presence of either Sb or Sb_2O_3.

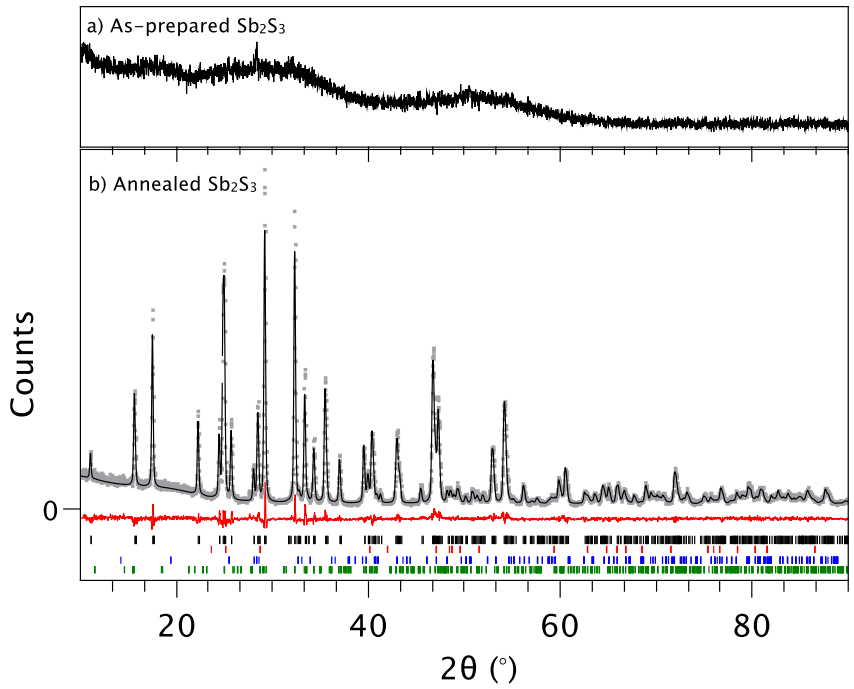

Figure 1 a) XRD pattern of as-prepared Sb_2S_3, b) XRD pattern of annealed Sb_2S_3 (grey circles), calculated Rietveld pattern (black line), difference between measured and calculated pattern (red line), Bragg positions for Sb_2S_3 (black vertical lines),[57] Sb (red vertical lines),[58] Sb_2O_3 (blue vertical lines),[59] orthorhombic sulfur (green vertical lines)[60]

Table 1 displays the determined parameters for the Rietveld refinement performed using the phase reference from Kyono and Kimata,[57] (orthorhombic *Pnma* space group, cell parameters, a=11.3197(9) Å, b=3.8332(2) Å, c=11.2330(8) Å). The refined lattice parameters showed good agreement with the literature values, indicating the success of the synthesis process. No non-Sb_2S_3 crystalline phase, including elemental antimony was found in the diffractogram. This suggests the complete reaction of the precursor material. With EDX spectroscopy (supplementary information, Figure S-4) the elemental compositions of the powder material before and after annealing were

measured. Both before and after annealing the material exhibited similar S:Sb atomic ratios, within 2 % of 3:2.

Table 1. Crystallographic parameters of synthesized Sb_2S_3 at room temperature, determined from XRD Rietveld refinement.

Sb_2S_3	*P n m a*		B_{ov} = 0.61(6) Å^2	
	a = 11.3168(4) Å	b = 3.8409(1) Å	c = 11.2384(4) Å	
	Wyckoff Position	*x*	*y*	*z*
Sb1	4c	0.4705(4)	¼	0.3257(4)
Sb2	4c	0.3503(4)	¾	0.0353(4)
S1	4c	0.289(1)	¼	0.191(1)
S2	4c	0.554(1)	¾	0.125(1)
S3	4c	0.376(1)	¾	0.442(1)
	χ^2 = 4.69	R_{Bragg} = 10.9	R_f = 7.24	

Qualitatively, the dispersions were capable of passing through a 0.22 μm PTFE syringe filter and remained stable, showing no aggregation or sedimentation for more than one month. Figure 2 displays the UV-Vis spectroscopic, DLS and zeta potential characterization of cleaned Sb_2S_3 solutions in methanol. The UV-Vis spectra, Figure 2a, shows a high degree of transparency, with a significant absorbance occurring below 600 nm, with complete absorption occurring in the ultraviolet region. The absorbance pattern agrees with the observed colour and transparency of the solution, with a lack of haze and precipitate suggesting a high-quality dispersion with minimal aggregation. To assess their electrostatic stability and suitability for EPD, the zeta potentials of the samples were measured. In methanol at an effective pH of 7.8, the zeta potential of the synthesized particles was measured at +52 mV (Figure 2b). A zeta potential of above +50 mV, or below -50 mV, indicates the sample is likely to be electrostatically stabilized, satisfying one of the

requirements for obtaining a good film by EPD.[45] The effective particle size in solution was measured by DLS as 115 nm with a dispersity of 0.07 (Figure 2c). The effective size in solution is increased due the presence of PEI, however is within the appropriate size-range for application in EPD.

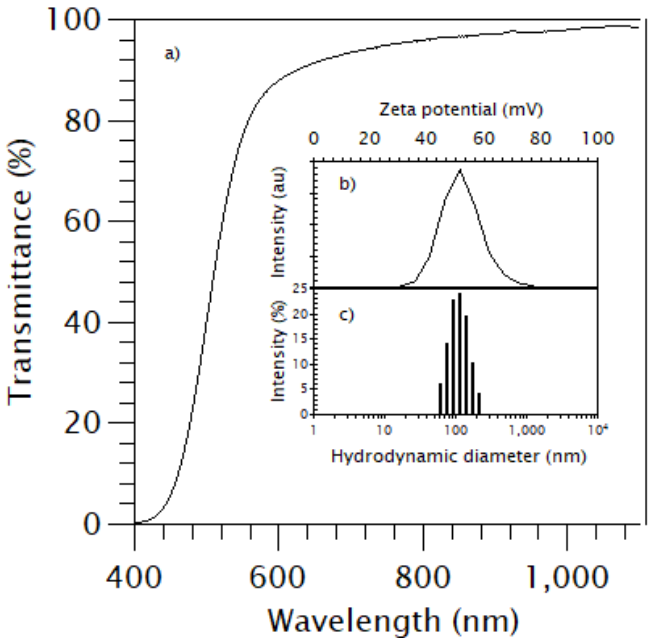

Figure 2. Properties of methanol-based solution of Sb_2S_3 with PEI, measured by a) UV-Vis spectroscopy, b) zeta potentiometry, c) size distribution analysis by DLS measurement

Films deposited out of methanol were prone to cracking while drying. Increasing the drying time reduced the incidence of cracking, however, to eliminate the cracking entirely film deposition was undertaken from a 1:1 by volume mixture of acetone and methanol. Acetone was found to improve the quality of the films, enabling rapid drying without visible cracking or defect formation. Films deposited for 1 minute or less showed good adhesion to the surface. Increasing the deposition time was found to increase the film thickness, however, also resulted in greater instances of crack and defect formation when drying. With extended deposition times the adhesion was poor, deposition times of approximately 5 minutes or more of continuous deposition resulted in delamination of the

layer from the surface, either spontaneously or when the sample was removed from the dispersion. When drying, thicker films were found to be prone to cracking, particularly at the sample edges, leading to poor quality films (supplementary information, Figure S-5).

Maintaining the deposition time at 1 minute and performing repeated depositions on the same surface was found to improve the quality of the films, and allowed for thicker films to be obtained before obvious film defects or delamination occurred. With this method, films of up to 1 μm were obtained. Figure 3 shows thin films of deposited Sb_2S_3 with PEI. Before annealing the films were yellow and transparent (Figure 3a), the SEM image (Figure 3b) of the film showed the surface, was smooth and uniform, without large aggregates present. Thin sections of annealed films are brown and transparent, while thicker sections tend towards dark grey and reflective (Figure 3c). The SEM image (Figures 3d and 3e) it can be seen that the Sb_2S_3 crystallized, forming a dense layer of overlapping rod-like antimony trisulfide, showing the characteristic needles expected for stibnite.

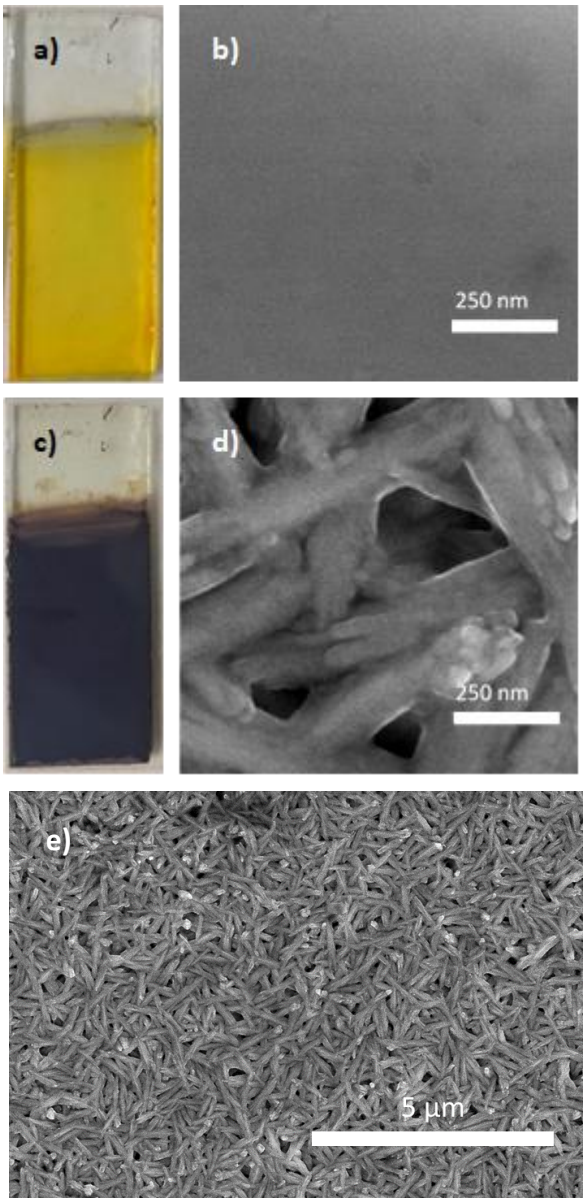

Figure 3. a) As-deposited (4x1 min) Sb_2S_3 thin film on ITO glass, b) SEM image of thin film of as-deposited film, c) annealed Sb_2S_3 thin film on ITO glass, d) SEM image of thin film of annealed Sb_2S_3 on ITO glass, e) larger scale SEM image of annealed Sb_2S_3 thin film on ITO glass

Both annealed and as-deposited films showed increasing thickness based on the number of depositions performed, as shown in Figure 4a. Films prepared with five repetitions or more began to show increasing defects, with cracking and peeling from the surface becoming evident. When

annealed, such defective films showed breakages and sections of complete delamination of the deposited layer. Annealed films were thinner than the as-deposited films as expected, reducing to approximately 58±4 %. After annealing the film profiles (Figure S-6) showed slightly increased roughness, potentially due to the presence of the rod-like crystalline structures on the surface. Amorphous antimony trisulfide thin films have been found to have a lower density than crystalline films,[61] contributing partially to the observed reduction in thickness. The remaining reduction can be attributed to the removal of the polymeric material during the annealing process.

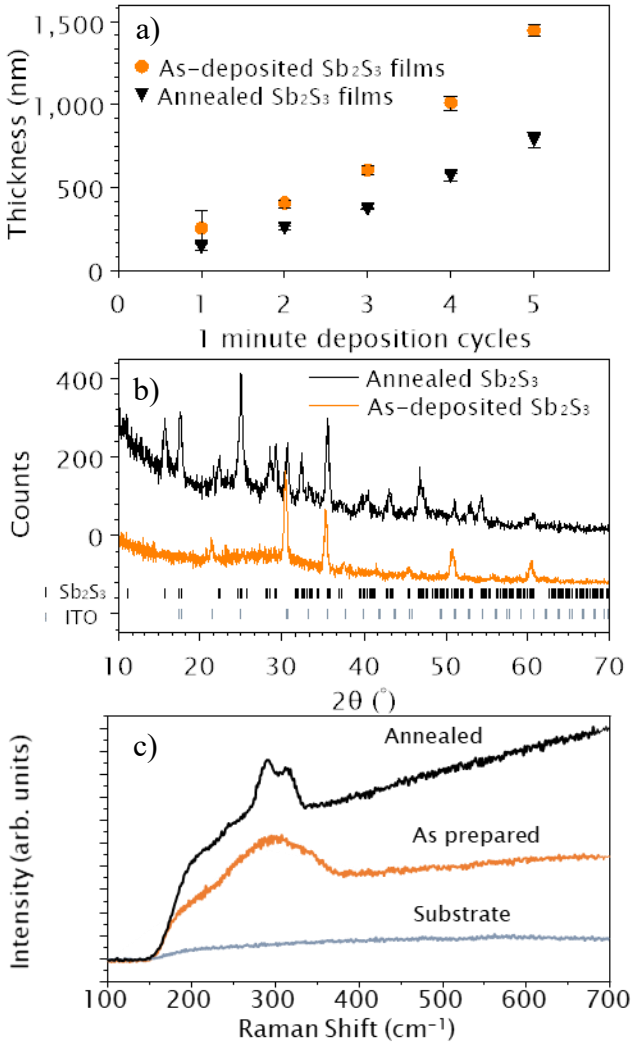

Figure 4. a) Film thickness of Sb_2S_3 thin films on ITO, measured by profilometry, b) XRD pattern obtained for thin film Sb_2S_3 on ITO glass (5×1 min), c) Raman spectra of pre- and post-annealing Sb_2S_3 thin films on ITO glass (5×1 min), and the spectrum of the underlying substrate

Elemental mapping of the films supported the non-uniformity introduced by the annealing process. As-prepared films (Figure S-9) showed an effectively uniform elemental distribution, with no sections revealing higher concentrations of antimony or sulfur, which would represent large particles as defects in the films, or silicon, indium, or tin, which would indicate thinner or porous sections of the films. After annealing the mapping (Figure S-10) shows sections with lower Sb and

S signals, and greater Si, In and Sn signals. These sections coincide with the pores and gaps introduced into the film due to the annealing process resulting in the reshaping of the amorphous particles into the rod-structured crystalline form.

Prior to annealing, the XRD pattern for the as-deposited thin films (Figure 4b) showed only peaks consistent with the presence of ITO glass. No peaks attributable to crystalline Sb_2S_3, Sb, or S_8 were present in the diffractogram. The XRD pattern obtained for the annealed thin film indicated the film consisted of Sb_2S_3, with the only other peaks present due to indium oxide within the ITO coating on the glass surface. No peaks due to antimony oxide were noted, nor were there peaks indicating the presence of elemental antimony or sulfur in the sample. This suggested that the EPD process, exposure to solvent, and subsequent annealing did not result in the oxidation of the sample, or the removal of significant quantities of sulfur.[30] Before annealing, the Raman spectra of the films (Figure 4c) showed a broad absorption between 200 and 400 cm^{-1}, consistent with what is expected for amorphous Sb_2S_3. After annealing two peaks at 290 and 315 cm^{-1} were observed. These peaks are consistent with Sb-S stretching modes of the crystalline phase of the Sb_2S_3.[30]

Photocurrent measurements of crystalline thin films showed a small stable photoelectric effect, (Figure 5), which is expected for Sb_2S_3. The semi-circular feature in the Nyquist plot (Figure S-7) shows a slight diameter reduction upon illumination, indicating the lowered resistance of the sample under illumination. Figure 5a shows time-responsive reproducible photocurrent response to illumination by different wavelengths over the range of 370-580 nm. It was observed that the highest photocurrent response occurred under illumination with 580 nm light. This wavelength-dependent response agrees with the reports of Zhang *et al.*[62] and Chao *et al.*[63]. It was observed (Figure S-8) that thicker films exhibited greater illuminated and dark currents, along with a greater

difference between the measured currents. Due to the method used to produce thicker films, namely by subsequent deposition of multiple layers, further study is required to assist in separating the effects of thickness, from the potential for the introduction of charge carriers from defects produced between adjacent Sb_2S_3 layers.

The UV-Vis-NIR spectra of the thin films of Sb_2S_3-PEI on ITO glass showed some of the optical differences between the as-deposited and annealed samples as expected (Figure 6). It was observed that the absorption edge of the solution (Figure 2) appears at the same wavelength as the as-deposited thin films. In the visible region, the overall transmittance of the samples was reduced upon annealing, with the onset of absorption occurring at a higher wavelength than the as-deposited samples, in agreement with Dong *et al*.[29] Within the NIR region of the spectrum resonant peaks were observed, showing correspondence to the number of produced film layers. The presence of these peaks is often attributed to high-quality films, with uniform thicknesses and without significant scattering or absorbance in the region of interest.[64,65] This transparency enables interference between the incident and reflected light leading to the presence of the absorbance peaks in the spectra.[66] The continued presence of the peaks through multiple deposition steps implies that the films deposited through multiple steps can be treated as a single large layer of the deposited material, rather than as multiple small layers of the antimony trisulfide and PEI.

The contrast between the complex refractive indices of as-deposited and annealed Sb_2S_3 was calculated (Figure 6c), from the n and k values extracted from the transmission spectra (Figure 6d). It was observed that the values for the extinction coefficient were low, with a low contrast between amorphous and crystalline values, while the refractive index showed higher values, and a contrast showing dependence on the film thickness, in agreement with results obtained for thin film Sb_2S_3 obtained by physical evaporation.[67] In the context of developing materials with

controllable optical properties for phase change applications, this shows the viability of EPD as a technique for tuning those optical properties during preparation.

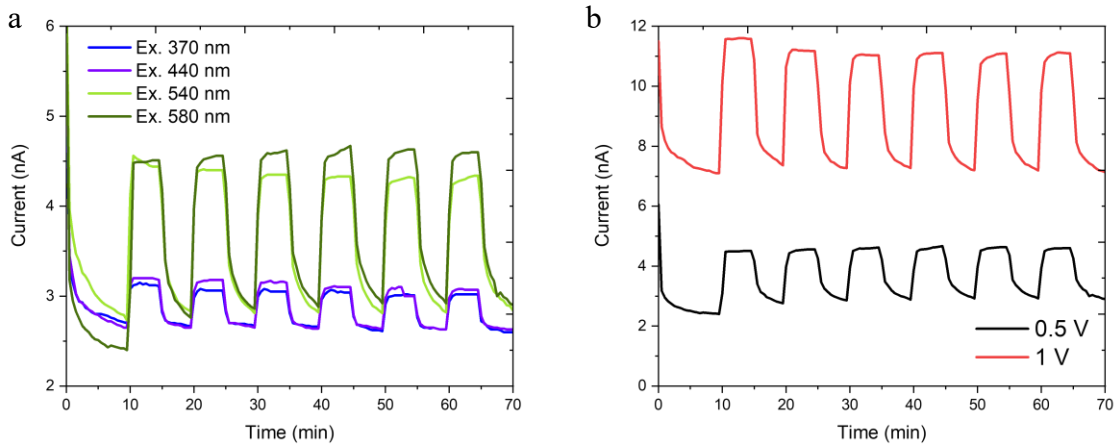

Figure 5. a) The dependence of the photocurrent intensity versus the exciting wavelength and b) The dependence of the photocurrent intensity versus the applied bias.

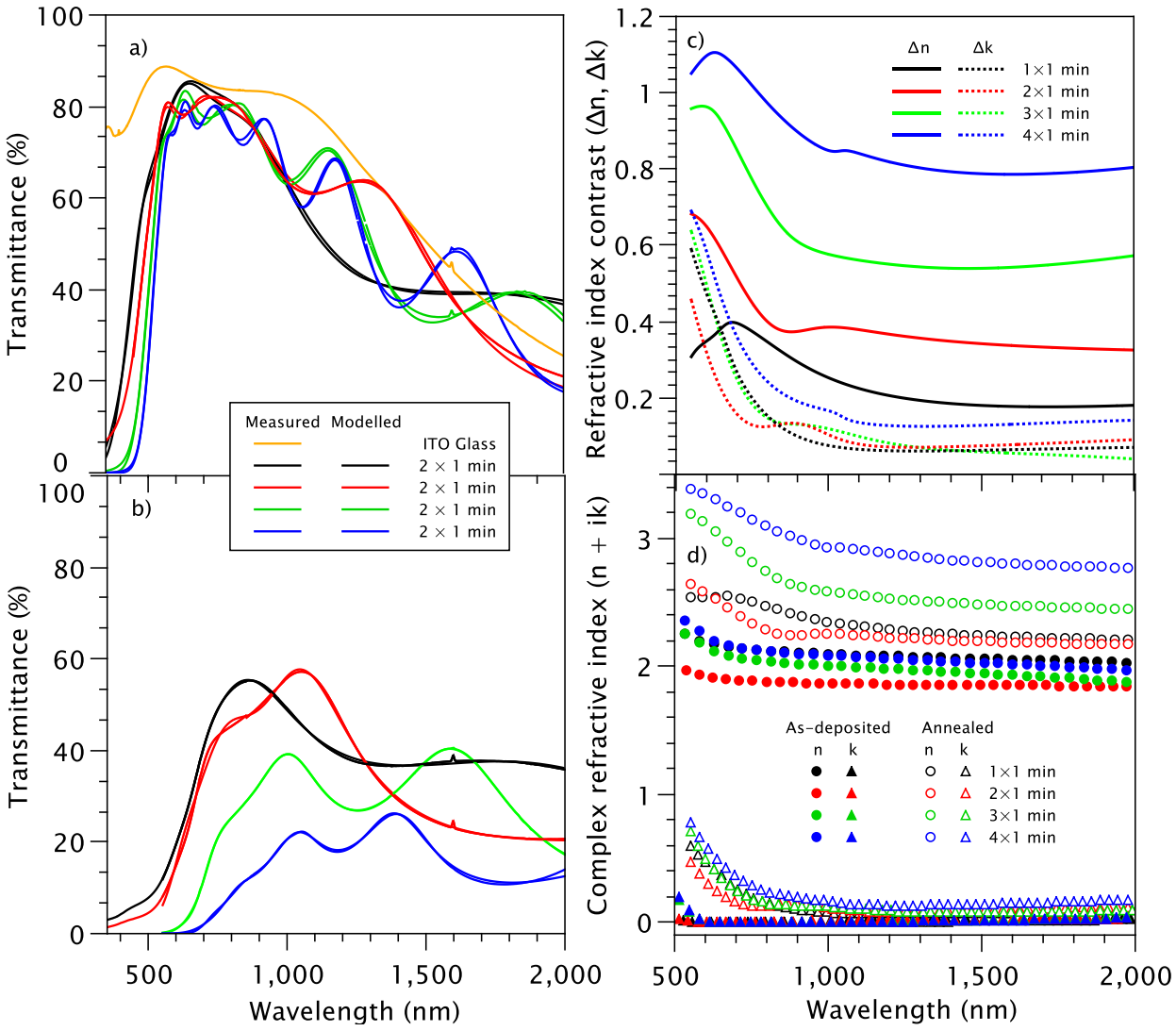

Figure 6. UV-Vis-NIR spectra, and associated modelled spectral profile, of thin films of Sb_2S_3, a) as-deposited, and b) after annealing at 300 °C for 1 hour under vacuum, c) plot of the contrast in complex refractive indices $\left(\Delta(n+ik) = \left(n_{annealed} - n_{as-deposited} + i\left(k_{annealed} - k_{as-deposited}\right)\right)\right.$ between as-deposited and annealed thin films of Sb_2S_3, d) complex refractive indices extracted from transmittance spectra of as-deposited and annealed Sb_2S_3 thin films.

The models prepared for the UV-Vis-NIR spectra of the thin films were able to reliably reproduce the observed transmittance data, with systematically low standard deviations

(approximately 1×10^{-4} or below). The fit of the ITO/glass system was very good with a thickness of 153 nm, and was used as the optical base in fitting the optical spectra of Sb_2S_3/ITO/glass bilayer films (as deposited and annealed films for various thicknesses). The thicknesses of the Sb_2S_3 layers were refined for each film with use of the optical interferences. The thicknesses, gap energies, plasma frequencies and carrier damping were deduced from the fitted spectra. The plasma frequency and carrier damping were used to determine the concentration and intrinsic mobility of the carriers in the Sb_2S_3 material for each thin film using equations (1) and (2) respectively. The carrier effective mass was taken as 0.4 for Sb_2S_3, as indicated by Shang *et al.*[68]

$$N = \frac{4\pi^2 C^2 \epsilon_0 m^*}{e^2} \Omega_p^2 \quad (1)$$

$$\mu = \frac{e}{2\pi C m^*} \cdot \frac{1}{\Omega_\tau} \quad (2)$$

Where N is the carrier concentration, C is the speed of light, ϵ_0 is vacuum permittivity, m^* is the carrier effective mass, e is the elementary charge, Ω_p is the plasma frequency, μ is the optical mobility, and Ω_τ is the damping constant.

Table 2. Measured and calculated values of as-deposited film properties measured and modelled using profilometry and UV-Vis-NIR spectrophotometry.

As-deposited *$m^*=0.4\ m_e$*

Dep. time (min)	Thickness, meas. (nm)	Thickness, model, (nm)	E_g (eV)	Ω_p (cm^{-1})	Carrier density (10^{20} cm^{-3})	Mobility ($cm^2 \cdot V^{-1} \cdot s^{-1}$)	σ, optical ($S \cdot cm^{-1}$)
1	257	165	2.2	2716	0.329	12.3	65
2	407	418	2.09	2730	0.333	2.37	13
3	605	613	2.14	3172	0.440	16.55	119
4	1008	884	2.14	2964	0.392	20.4	128

Table 3. Measured and calculated values of annealed film properties measured and modelled using profilometry and UV-Vis-NIR spectrophotometry.

Annealed (300 °C, 1 hour, under vacuum) *$m^*=0.4\ m_e$*

Dep. time (min)	Thickness, meas. (nm)	Thickness, model, (nm)	E_g (eV)	Ω_p (cm^{-1})	Carrier density (10^{20} cm^{-3})	Mobility ($cm^2 \cdot V^{-1} \cdot s^{-1}$)	σ, optical ($S \cdot cm^{-1}$)
1	142	130	1.27	12106	6.55	2.34	245
2	254	225	1.47	12911	7.45	2.97	354
3	372	383	1.43	14426	9.30	1.43	213
4	564	515	1.44	10561	4.99	1.43	112

Tables 2 and 3 reports the given values of thicknesses, band gap energy (E_g), plasma frequency (Ω_p), carrier mobility and the expected calculated electrical conductivity (σ) for each sample. The thicknesses determined by the model are in agreement with the values measured by profilometry. From the model it was deduced that the band gap energy decreases after the annealing step (from 2.15±0.05 eV to 1.4±0.1 eV). The band gap energy of the as-deposited sample is close to those reported by some studies devoted to the photovoltaic application of Sb_2S_3,[69] while the post-annealing band gaps show values closer to those calculated by M.R. Filip et al.[23] and T. Ben Nasr et al.[24] by DFT calculation. The annealing step may have reduced the tensile strains induced in the Sb_2S_3 films due to the substrate-as-deposited film mismatch leading to a band gap energy closer to that of the unstressed crystal.

The decreased bandgap with annealing also suggests an explanation for the increased carrier concentration upon crystallization. Thermal excitation of carriers across the bandgap will become more attainable upon reduction of the bandgap, increasing the carrier concentration of the material at high temperature which was observed in all samples upon annealing. The best expected

electrical conductivity of annealed samples was obtained for low global deposition times. The samples showed an increase in carrier density when annealed, increasing from ~3-4×10^{19} cm^{-3}, to ~5-9×10^{20} cm^{-3}. Upon annealing the plasma frequency increased significantly, indicating the presence of many charge carriers, however the low conductivity, and low carrier mobilities measured during photocurrent measurements suggests a hopping transport mode of conductivity.[67] The limited increase in conductivity observed is likely limited by the barrier potential of the hopping mechanism and carrier trapping, reflected by the lowering in conductor mobility during annealing, however further studies,[70] and in particular elevated temperature conductivity studies would be required to further elucidate the mechanism. The suggested model serves as a useful approximation for the samples, however indicates the need for further analysis into the optoelectronic properties of thin film Sb_2S_3.

Conclusions

Transparent thin films of Sb_2S_3 with phase-dependent optoelectronic properties were prepared by EPD. The synthetic method was optimized specifically for application with EPD, using PEI; as a capping and stabilizing agent during synthesis, a charge-bearing moiety during deposition, and as a binder after film formation. Robust, transparent films were obtained with thicknesses ranging up to 1 μm, and optical properties based on that thickness. Annealed films showed excellent adhesion to the surface, resistant to physical removal and dissolution. Annealing of the films was able to induce the phase change from amorphous to crystalline, without the formation of antimony oxide as a by-product, as indicated by the XRD patterns obtained. The agreement between the simulated and obtained UV-Vis spectrum was sufficiently good as to enable the extraction of the

band gap energies for both forms, showing good agreement with values obtained from films prepared by other means.

This work demonstrates the viability of tailoring wet-chemical syntheses of nanoparticles specifically for EPD based deposition processes. Through the careful selection of stabilizing agent, functional nanoparticles can be directly deposited with only a simple washing step after synthesis. The successful application of EPD for the production of PCM thin films is a promising step towards their application, enabling the rapid production of uniform thin films, with inexpensive, readily available hardware, and chemical precursors.

Associated Content

Supporting Information.

Supplementary material: Diagram of photocurrent measurement apparatus, images of syntheses, synthesised powders, EDX spectra of powder, images of poor film depositions, thickness profiles of thin films, additional photocurrent measurement data (Nyquist and time plots), EDX mapping of thin films, optical model description. File: SupportingInformation.docx (PDF)

Author Information

Author Contributions

The manuscript was written through contributions of all authors. All authors have given approval to the final version of the manuscript.

Acknowledgements

The authors would like to acknowledge funding from CNRS Emergence program. C.L.H., B. S. and F. S. acknowledge the Japan Society for the Promotion of Science for postdoctoral fellowships

JSPS P21723, P19720 and P18797, and KAKENHI JP19F19720, JP18F18797, respectively. Support from JST JPMJMI19A1 is also gratefully acknowledged.

Notes

The authors declare no competing financial interest.

References

(1) Wuttig, M.; Raoux, S. The Science and Technology of Phase Change Materials. *Zeitschrift für Anorg. und Allg. Chemie* **2012**, *638* (15), 2455–2465.

(2) Noé, P.; Vallée, C.; Hippert, F.; Fillot, F.; Raty, J. Y. Phase-Change Materials for Non-Volatile Memory Devices: From Technological Challenges to Materials Science Issues. *Semiconductor Science and Technology*. Institute of Physics Publishing January 1, 2018, p 32.

(3) Delaney, M.; Zeimpekis, I.; Lawson, D.; Hewak, D. W.; Muskens, O. L. A New Family of Ultralow Loss Reversible Phase-Change Materials for Photonic Integrated Circuits: Sb_2S_3 and Sb_2Se_3. *Adv. Funct. Mater.* **2020**, *30* (36), 2002447.

(4) Maier, S.; Hebert, S.; Kabbour, H.; Pelloquin, D.; Perez, O.; Berthebaud, D.; Gascoin, F. Synthesis, Electronic Structure and Physical Properties of Polycrystalline $Ba_2FePnSe_5$ (Pn = Sb, Bi). *Mater. Chem. Phys.* **2018**, *203*, 202–211.

(5) Michel, A.-K. U.; Sousa, M.; Yarema, M.; Yarema, O.; Ovuka, V.; Lassaline, N.; Wood, V.; Norris, D. J. Optical Properties of Amorphous and Crystalline GeTe Nanoparticle Thin Films: A Phase-Change Material for Tunable Photonics. *ACS Appl. Nano Mater.* **2020**, *3* (5), 4314–4320.

(6) Gemo, E.; Faneca, J.; G.-C. Carrillo, S.; Baldycheva, A.; Pernice, W. H. P.; Bhaskaran, H.; Wright, C. D. A Plasmonically Enhanced Route to Faster and More Energy-Efficient Phase-Change Integrated Photonic Memory and Computing Devices. *J. Appl. Phys.* **2021**, *129* (11), 110902.

(7) Wuttig, M.; Yamada, N. Phase-Change Materials for Rewriteable Data Storage. *Nat. Mater.* **2007**, *6* (11), 824–832.

(8) Wuttig, M.; Bhaskaran, H.; Taubner, T. Phase-Change Materials for Non-Volatile Photonic Applications. *Nat. Photonics* **2017**, *11* (8), 465–476.

(9) Saito, Y.; Fons, P.; Kolobov, A. V; Mitrofanov, K. V; Makino, K.; Tominaga, J.; Hatayama, S.; Sutou, Y.; Hase, M.; Robertson, J. High-Quality Sputter-Grown Layered Chalcogenide Films for Phase Change Memory Applications and Beyond. *J. Phys. D. Appl. Phys.* **2020**, *53* (28), 284002.

(10) Hosseini, P.; Wright, C. D.; Bhaskaran, H. An Optoelectronic Framework Enabled by Low-Dimensional Phase-Change Films. *Nature* **2014**, *511* (7508), 206–211.

(11) Zhang, Y.; Chou, J. B.; Li, J.; Li, H.; Du, Q.; Yadav, A.; Zhou, S.; Shalaginov, M. Y.; Fang, Z.; Zhong, H.; Roberts, C.; Robinson, P.; Bohlin, B.; Ríos, C.; Lin, H.; Kang, M.; Gu, T.; Warner, J.; Liberman, V.; Richardson, K.; Hu, J. Broadband Transparent Optical Phase Change Materials for High-Performance Nonvolatile Photonics. *Nat. Commun.* **2019**, *10* (1), 4279.

(12) Raeis-Hosseini, N.; Rho, J. Metasurfaces Based on Phase-Change Material as a Reconfigurable Platform for Multifunctional Devices. *Materials (Basel).* **2017**, *10* (9),

1046.

(13) Wang, Q.; Rogers, E. T. F.; Gholipour, B.; Wang, C.-M.; Yuan, G.; Teng, J.; Zheludev, N. I. Optically Reconfigurable Metasurfaces and Photonic Devices Based on Phase Change Materials. *Nat. Photonics* **2016**, *10* (1), 60–65.

(14) Perumal, S.; Roychowdhury, S.; Biswas, K. High Performance Thermoelectric Materials and Devices Based on GeTe. *J. Mater. Chem. C* **2016**, *4* (32), 7520–7536.

(15) Lee, B.-S.; Abelson, J. R.; Bishop, S. G.; Kang, D.-H.; Cheong, B.; Kim, K.-B. Investigation of the Optical and Electronic Properties of $Ge_2Sb_2Te_5$ Phase Change Material in Its Amorphous, Cubic, and Hexagonal Phases. *J. Appl. Phys.* **2005**, *97* (9), 93509.

(16) Abdollahramezani, S.; Hemmatyar, O.; Taghinejad, H.; Krasnok, A.; Kiarashinejad, Y.; Zandehshahvar, M.; Alù, A.; Adibi, A. Tunable Nanophotonics Enabled by Chalcogenide Phase-Change Materials. *Nanophotonics* **2020**, *9* (5), 1189–1241.

(17) Michel, A.-K. U.; Wuttig, M.; Taubner, T. Design Parameters for Phase-Change Materials for Nanostructure Resonance Tuning. *Adv. Opt. Mater.* **2017**, *5* (18), 1700261.

(18) Carrillo, S. G.-C.; Trimby, L.; Au, Y.-Y.; Nagareddy, V. K.; Rodriguez-Hernandez, G.; Hosseini, P.; Ríos, C.; Bhaskaran, H.; Wright, C. D. A Nonvolatile Phase-Change Metamaterial Color Display. *Adv. Opt. Mater.* **2019**, *7* (18), 1801782.

(19) Srinivasan, B.; Berthebaud, D.; Mori, T. Is LiI a Potential Dopant Candidate to Enhance the Thermoelectric Performance in Sb-Free GeTe Systems? A Prelusive Study. *Energies* **2020**, *13* (3), 643.

(20) Srinivasan, B.; Le Tonquesse, S.; Gellé, A.; Bourgès, C.; Monier, L.; Ohkubo, I.; Halet, J.

F.; Berthebaud, D.; Mori, T. Screening of Transition (Y, Zr, Hf, V, Nb, Mo, and Ru) and Rare-Earth (La and Pr) Elements as Potential Effective Dopants for Thermoelectric GeTe - an Experimental and Theoretical Appraisal. *J. Mater. Chem. A* **2020**, *8* (38), 19805–19821.

(21) Rajpure, K. Y.; Lokhande, C. D.; Bhosale, C. H. A Comparative Study of Concentration Effect of Complexing Agent on the Properties of Spray Deposited Sb_2S_3 Thin Films and Precipitated Powders. *Mater. Chem. Phys.* **1997**, *51* (3), 252–257.

(22) Mahanty, S.; Merino, J. M.; León, M. Preparation and Optical Studies on Flash Evaporated Sb_2S_3 Thin Films. *J. Vac. Sci. Technol. A Vacuum, Surfaces Film.* **1997**, *15* (6), 3060–3064.

(23) Filip, M. R.; Patrick, C. E.; Giustino, F. G W Quasiparticle Band Structures of Stibnite, Antimonselite, Bismuthinite, and Guanajuatite. *Phys. Rev. B* **2013**, *87* (20), 205125.

(24) Nasr, T. Ben; Maghraoui-Meherzi, H.; Abdallah, H. Ben; Bennaceur, R. Electronic Structure and Optical Properties of Sb_2S_3 Crystal. *Phys. B Condens. Matter* **2011**, *406* (2), 287–292.

(25) Syzrantsev, V. V.; Zavyalov, a. P.; Bardakhanov, S. P. The Role of Associated Liquid Layer at Nanoparticles and Its Influence on Nanofluids Viscosity. *Int. J. Heat Mass Transf.* **2014**, *72*, 501–506.

(26) Koc, H.; Mamedov, A. M.; Deligoz, E.; Ozisik, H. First Principles Prediction of the Elastic, Electronic, and Optical Properties of Sb_2S_3 and Sb_2Se_3 Compounds. *Solid State Sci.* **2012**, *14* (8), 1211–1220.

(27) Maghraoui-Meherzi, H.; Nasr, T. Ben; Kamoun, N.; Dachraoui, M. Physical Properties of Chemically Deposited Sb2S3 Thin Films. *Comptes Rendus Chim.* **2011**, *14* (5), 471–475.

(28) Arun, P.; Vedeshwar, A. G. Effect of Heat Treatment on the Optical Properties of Amorphous Sb2S3 Film: The Possibility of Optical Storage. *J. Non. Cryst. Solids* **1997**, *220* (1), 63–68.

(29) Dong, W.; Liu, H.; Behera, J. K.; Lu, L.; Ng, R. J. H.; Sreekanth, K. V.; Zhou, X.; Yang, J. K. W.; Simpson, R. E. Wide Bandgap Phase Change Material Tuned Visible Photonics. *Adv. Funct. Mater.* **2019**, *29* (6), 1806181.

(30) Parize, R.; Cossuet, T.; Chaix-Pluchery, O.; Roussel, H.; Appert, E.; Consonni, V. In Situ Analysis of the Crystallization Process of Sb_2S_3 Thin Films by Raman Scattering and X-Ray Diffraction. *Mater. Des.* **2017**, *121*, 1–10.

(31) DeAngelis, A. D.; Kemp, K. C.; Gaillard, N.; Kim, K. S. Antimony(III) Sulfide Thin Films as a Photoanode Material in Photocatalytic Water Splitting. *ACS Appl. Mater. Interfaces* **2016**, *8* (13), 8445–8451.

(32) Mills, K. C. Thermodynamic Data for Inorganic Sulphides, Selenides and Tellurides. **1974**.

(33) Ji, X.; Wu, L.; Zhou, W.; Zhu, M.; Rao, F.; Song, Z.; Cao, L.; Feng, S. High Thermal Stability Sb_3Te-TiN_2 Material for Phase Change Memory Application. *Appl. Phys. Lett.* **2015**, *106* (2), 23118.

(34) Yang, H.; Li, M.; Fu, L.; Tang, A.; Mann, S. Controlled Assembly of Sb_2S_3 Nanoparticles on Silica/Polymer Nanotubes: Insights into the Nature of Hybrid Interfaces. *Sci. Rep.* **2013**, *3*, 1336.

(35) Zhu, J.; Yan, X.; Cheng, J. Synthesis of Water-Soluble Antimony Sulfide Quantum Dots and Their Photoelectric Properties. *Nanoscale Res. Lett.* **2018**, *13* (1), 19.

(36) Dutková, E.; Takacs, L.; Sayagués, M. J.; Baláž, P.; Kováč, J.; Šatka, A. Mechanochemical Synthesis of Sb2S3 and Bi2S3 Nanoparticles. *Chem. Eng. Sci.* **2013**, *85*, 25–29.

(37) Cavalleri, A.; Tóth, C.; Siders, C. W.; Squier, J. A.; Ráksi, F.; Forget, P.; Kieffer, J. C. Femtosecond Structural Dynamics in VO_2 during an Ultrafast Solid-Solid Phase Transition. *Phys. Rev. Lett.* **2001**, *87* (23), 237401.

(38) Lotnyk, A.; Behrens, M.; Rauschenbach, B. Phase Change Thin Films for Non-Volatile Memory Applications. *Nanoscale Adv.* **2019**, *1* (10), 3836–3857.

(39) Liu, H.; Dong, W.; Wang, H.; Lu, L.; Ruan, Q.; Tan, Y. S.; Simpson, R. E.; Yang, J. K. W. Rewritable Color Nanoprints in Antimony Trisulfide Films. *Sci. Adv.* **2020**, *6* (51), eabb7171.

(40) Raoux, S.; Jordan-Sweet, J. L.; Kellock, A. J. Crystallization Properties of Ultrathin Phase Change Films. *J. Appl. Phys.* **2008**, *103* (11), 114310.

(41) Noé, P.; Sabbione, C.; Bernier, N.; Castellani, N.; Fillot, F.; Hippert, F. Impact of Interfaces on Scenario of Crystallization of Phase Change Materials. *Acta Mater.* **2016**, *110*, 142–148.

(42) Tang, R.; Chen, X.; Luo, Y.; Chen, Z.; Liu, Y.; Li, Y.; Su, Z.; Zhang, X.; Fan, P.; Liang, G. Controlled Sputtering Pressure on High-Quality Sb_2Se_3 Thin Film for Substrate Configurated Solar Cells. *Nanomaterials* **2020**, *10* (3), 574.

(43) Castro, J. R.-; Dale, P.; Mahon, M. F.; Molloy, K. C.; Peter, L. M. Deposition of Antimony Sulfide Thin Films from Single-Source Antimony Thiolate Precursors. *Chem. Mater.* **2007**, *19* (13), 3219–3226.

(44) Yesugade, N. S.; Lokhande, C. D.; Bhosale, C. H. Structural and Optical Properties of

Electrodeposited Bi_2S_3, Sb_2S_3 and As_2S_3 Thin Films. *Thin Solid Films* **1995**, *263* (2), 145–149.

(45) Besra, L.; Liu, M. A Review on Fundamentals and Applications of Electrophoretic Deposition (EPD). *Prog. Mater. Sci.* **2007**, *52* (1), 1–61.

(46) Lai, Y.; Tang, Y.; Gong, J.; Gong, D.; Chi, L.; Lin, C.; Chen, Z. Transparent Superhydrophobic/Superhydrophilic TiO_2-Based Coatings for Self-Cleaning and Anti-Fogging. *J. Mater. Chem.* **2012**, *22* (15), 7420–7426.

(47) Renaud, A.; Nguyen, T. K. N.; Grasset, F.; Raissi, M.; Guillon, V.; Delabrouille, F.; Dumait, N.; Jouan, P.-Y.; Cario, L.; Jobic, S.; Pellegrin, Y.; Odobel, F.; Cordier, S.; Uchikoshi, T. Preparation by Electrophoretic Deposition of Molybdenum Iodide Cluster-Based Functional Nanostructured Photoelectrodes for Solar Cells. *Electrochim. Acta* **2019**, *317*, 737–745.

(48) Thi Kim Nguyen, N.; Dubernet, M.; Matsui, Y.; Wilmet, M.; Shirahata, N.; Rydzek, G.; Dumait, N.; Amela-Cortes, M.; Renaud, A.; Cordier, S. Transparent Functional Nanocomposite Films Based on Octahedral Metal Clusters: Synthesis by Electrophoretic Deposition Process and Characterization. *R. Soc. open Sci.* **2019**, *6* (3), 181647.

(49) Ryu, S.; Kwon, Y. J.; Kim, Y.; Lee, J. U. Corrosion Protection Coating of Three-Dimensional Metal Structure by Electrophoretic Deposition of Graphene Oxide. *Mater. Chem. Phys.* **2020**, *250*, 123039.

(50) Uchikoshi, T.; Kreethawate, L.; Matsunaga, C.; Larpkiattaworn, S.; Jiemsirilers, S.; Besra, L. Fabrication of Ceramic Membranes on Porous Ceramic Supports by Electrophoretic

Deposition. *Adv. Appl. Ceram.* **2014**, *113* (1), 3–7.

(51) Huma, Z.-E.; Gupta, A.; Javed, I.; Das, R.; Hussain, S. Z.; Mumtaz, S.; Hussain, I.; Rotello, V. Cationic Silver Nanoclusters as Potent Antimicrobials against Multidrug-Resistant Bacteria. *ACS Omega* **2018**, *3*, 16721–16727.

(52) Roisnel, T.; Rodríquez-Carvajal, J. WinPLOTR: A Windows Tool for Powder Diffraction Pattern Analysis. *Mater. Sci. Forum* **2001**, *378* (1), 118–123.

(53) Rodriguez-Carvajal, J.; Roisnel, T. FullProf. 98 and WinPLOTR: New Windows 95/NT Applications for Diffraction. *Comm. Powder Diffraction, Int. Union Crystallogr. Newsl.* **1998**, *20*, May-August.

(54) Rodríguez-Carvajal, J. Recent Advances in Magnetic Structure Determination by Neutron Powder Diffraction. *Phys. B* **1993**, *192* (1–2), 55–69.

(55) Theiß, W. Theiss Hard-and Software for Optical Spectroscopy. *Dr. Bernhard-Klein-Str* **2004**, *110*, 52078.

(56) Demichelis, F.; Kaniadakis, G.; Tagliaferro, A.; Tresso, E. New Approach to Optical Analysis of Absorbing Thin Solid Films. *Appl. Opt.* **1987**, *26* (9), 1737–1740.

(57) Kyono, A.; Kimata, M. Structural Variations Induced by Difference of the Inert Pair Effect in the Stibnite-Bismuthinite Solid Solution Series $(Sb,Bi)_2S_3$. *Am. Mineral.* **2004**, *89* (7), 932–940.

(58) Barrett, C. S.; Cucka, P.; Haefner, K. The Crystal Structure of Antimony at 4.2, 78 and 298 K. *Acta Crystallogr.* **1963**, *16* (6), 451–453.

(59) Svensson, C. The Crystal Structure of Orthorhombic Antimony Trioxide, Sb2O3. *Acta Crystallogr. Sect. B Struct. Crystallogr. Cryst. Chem.* **1974**, *30* (2), 458–461.

(60) Abrahams, S. C. The Crystal and Molecular Structure of Orthorhombic Sulfur. *Acta Crystallogr.* **1955**, *8* (11), 661–671.

(61) Kaito, C.; Nakamura, N.; Yoshida, T.; Shiojiri, M. Structure and the Process of Crystallization in Thin Amorphous Sb2S3 Films. *J. Cryst. Growth* **1984**, *66* (1), 156–162.

(62) Zhang, K.; Luo, T.; Chen, H.; Lou, Z.; Shen, G. Au-Nanoparticles-Decorated Sb_2S_3 Nanowire-Based Flexible Ultraviolet/Visible Photodetectors. *J. Mater. Chem. C* **2017**, *5* (13), 3330–3335.

(63) Chao, J.; Liang, B.; Hou, X.; Liu, Z.; Xie, Z.; Liu, B.; Song, W.; Chen, G.; Chen, D.; Shen, G. Selective Synthesis of Sb_2S_3 Nanoneedles and Nanoflowers for High Performance Rigid and Flexible Photodetectors. *Opt. Express* **2013**, *21* (11), 13639–13647.

(64) Caglar, M.; Çağlar, Y.; Ilican, S. The Determination of the Thickness and Optical Constants of the ZnO Crystalline Thin Film by Using Envelope Method. *J. Optoelectron. Adv. Mater.* **2006**, *8*, 1410–1413.

(65) Yoshino, H.; Abbas, A.; Kaminski, P. M.; Smith, R.; Walls, J. M.; Mansfield, D. Measurement of Thin Film Interfacial Surface Roughness by Coherence Scanning Interferometry. *J. Appl. Phys.* **2017**, *121* (10), 105303.

(66) Nguyen, T. K. N.; Grasset, F.; Dierre, B.; Matsunaga, C.; Cordier, S.; Lemoine, P.; Ohashi, N.; Uchikoshi, T. Fabrication of Transparent Thin Film of Octahedral Molybdenum Metal Clusters by Electrophoretic Deposition. *ECS J. Solid State Sci. Technol.* **2016**, *5* (10), R178–

R186.

(67) Zaki, S. A.; Abd-Elrahman, M. I.; Abu-Sehly, A. A. Optical and Electrical Properties of Amorphous Sb2S3 Thin Films: Effect of the Film Thickness. *J. Non. Cryst. Solids* **2021**, *552*, 120318.

(68) Shang, M. H.; Zhang, J.; Wei, S.; Zhu, Y.; Wang, L.; Hou, H.; Wu, Y.; Fujikawa, T.; Ueno, N. Bi-Doped Sb_2S_3 for Low Effective Mass and Optimized Optical Properties. *J. Mater. Chem. C* **2016**, *4* (22), 5081–5090.

(69) Mane, R. S.; Lokhande, C. D. Thickness-Dependent Properties of Chemically Deposited Sb_2S_3 Thin Films. *Mater. Chem. Phys.* **2003**, *82* (2), 347–354.

(70) Yang, Z.; Wang, X.; Chen, Y.; Zheng, Z.; Chen, Z.; Xu, W.; Liu, W.; Yang, Y. (Michael); Zhao, J.; Chen, T.; Zhu, H. Ultrafast Self-Trapping of Photoexcited Carriers Sets the Upper Limit on Antimony Trisulfide Photovoltaic Devices. *Nat. Commun.* **2019**, *10* (1), 4540.

Table of contents graphic

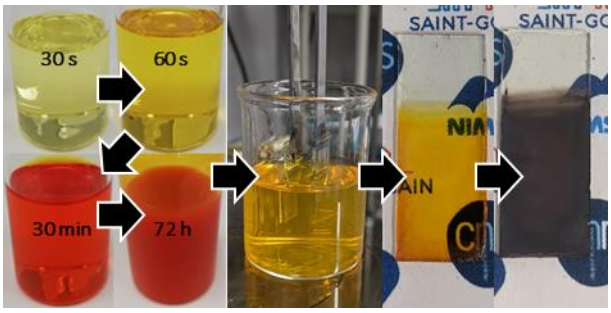

Summary statement

Polyethyleneimine-stabilised Sb_2S_3 nanoparticles are synthesised, prepared as thin-films via electrophoretic deposition, and their physical and optoelectronic properties evaluated in amorphous and crystalline states.